

# Reversal of triboelectric charges on sol-gel oxide films annealed at different temperatures

Cite as: Appl. Phys. Lett. **118**, 243902 (2021); <https://doi.org/10.1063/5.0055312>

Submitted: 27 April 2021 . Accepted: 27 May 2021 . Published Online: 15 June 2021

Yongqiao Zhu, Shiquan Lin, Wenchao Gao, Miao Zhang, Dawei Li, Peizhong Feng,  Cheng Xu, and Zhong Lin Wang



View Online



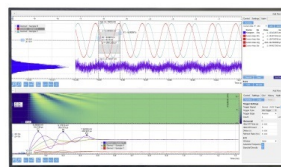
Export Citation



CrossMark

## Challenge us.

What are your needs for periodic signal detection?



Zurich  
Instruments



# Reversal of triboelectric charges on sol-gel oxide films annealed at different temperatures

Cite as: Appl. Phys. Lett. **118**, 243902 (2021); doi: [10.1063/5.0055312](https://doi.org/10.1063/5.0055312)

Submitted: 27 April 2021 · Accepted: 27 May 2021 ·

Published Online: 15 June 2021




View Online



Export Citation



CrossMark

Yongqiao Zhu,<sup>1</sup> Shiquan Lin,<sup>2</sup> Wenchao Gao,<sup>3</sup> Miao Zhang,<sup>1</sup> Dawei Li,<sup>4</sup> Peizhong Feng,<sup>1</sup> Cheng Xu,<sup>1,2,a)</sup> and Zhong Lin Wang<sup>2,5,a)</sup> 

## AFFILIATIONS

<sup>1</sup>School of Materials Science and Engineering, China University of Mining and Technology, Xuzhou 221116, China

<sup>2</sup>CAS Center for Excellence in Nanoscience, Beijing Key Laboratory of Micro-Nano Energy and Sensor, Beijing Institute of Nanoenergy and Nanosystems, Chinese Academy of Sciences, Beijing 100083, China

<sup>3</sup>Department of Civil Engineering, Monash University, 3800 Clayton, Australia

<sup>4</sup>Key Laboratory of Materials for High Power Laser, Shanghai Institute of Optics and Fine Mechanics, Chinese Academy of Sciences, Shanghai 201800, China

<sup>5</sup>School of Materials Science and Engineering, Georgia Institute of Technology, Atlanta, Georgia 30332-0245, USA

<sup>a)</sup>Authors to whom correspondence should be addressed: [xucheng@cumt.edu.cn](mailto:xucheng@cumt.edu.cn) and [zhong.wang@mse.gatech.edu](mailto:zhong.wang@mse.gatech.edu)

## ABSTRACT

Using Kelvin probe force microscopy, we studied the contact-electrification (CE) induced charge density on the surfaces of organic-inorganic composite oxide films, such as Nb<sub>2</sub>O<sub>5</sub>, ZrO<sub>2</sub>, and HfO<sub>2</sub> films, prepared by a sol-gel method and annealed at different temperatures. The results show that positive triboelectric charges on the film surface gradually turn into negative ones with the increase in the annealing temperature. This phenomenon is attributed to the broken valence bonds between organics and organic-inorganic composites in the film at high temperature, which causes oxygen vacancy defects and consequently changes the surface states of the film. A surface states model is established to understand the process of CE, which further confirms that electron transfer is the dominant mechanism of CE. Moreover, it indicates that in addition to oxygen vacancies, there are also many other factors that can influence CE, including but not limited to non-stoichiometric ratios, impurities, and other types of defects. These factors will modify the surface states through changing the potential barrier energy of the bound electrons on the surface and thus impact the amount and even the direction of electron transfer.

Published under an exclusive license by AIP Publishing. <https://doi.org/10.1063/5.0055312>

As an emerging technology based on contact-electrification (CE) and electrostatic induction, the triboelectric nanogenerator (TENG) has been providing people with an option to solve the world's energy problems.<sup>1-3</sup> In the meantime, its wide range applications draw people's attention to explore the mechanism of CE, which is a well-known but not clearly understood effect.<sup>4-6</sup>

CE has generally been explained by three types of mechanisms in history, namely, electron transfer, ion transfer, and material transfer.<sup>7-9</sup> Among these mechanisms, in recent years, electron transfer was extensively highlighted and rigorously validated on both macroscopic and microscopic scales. For instance, a macroscopic CE mechanism was explored through introducing the initial charges and observing evolution characteristics of the surface charge density/amount of TENG under different temperature conditions over time.<sup>10,11</sup> The results were in good agreement with the thermionic emission model, confirming the fundamental role of electron transfer in CE between

two different solid materials. Based on this, efforts were made to suppress thermionic emission and further develop the high temperature-resistant TENG at 673 K, which revealed a universal CE mechanism with consideration of temperature effects.<sup>12</sup> In terms of research on the microscopic CE mechanism, bias voltages were acted on Kelvin probe force microscopy (KPFM) to control the quantity and characteristic of the generated charges.<sup>13</sup> In addition, it was found that there existed a threshold photon energy for releasing the triboelectric charges from the dielectric surface under photon excitation, which was attributed to the photoelectron emission of the charges trapped in the surface states of the dielectric material.<sup>14</sup> The KPFM-based charge transfer process at the nanoscale was also found to follow the modified thermionic emission model under the high temperature conditions.<sup>15</sup> In previous studies, one of the key findings was the determination of the role of electron transfer in CE under the high temperature conditions. Materials involved in these studies were mainly high

temperature-resistant semiconductors or insulators, while polymers, even for those with high temperature-resistant properties, were subjected to the damages of electrification characteristics on their surfaces.<sup>16,17</sup>

In this study, different organic–inorganic composite oxide films are prepared by the sol–gel method. They are first annealed at different temperatures and then placed on the KPFM for observation of changes in triboelectric charge quantities and characteristics at the ambient condition. Some details about the preparation, characterization, and treatment can be found in the [supplementary material](#).

The sol–gel films were prepared on a highly doped Si substrate, and the triboelectric charges were generated by scanning a Pt coated tip on the surface using the KPFM setup [Fig. 1(a)]. Specifically, Nb<sub>2</sub>O<sub>5</sub> films were prepared with NbCl<sub>5</sub> as the precursor, followed by annealing at respective temperatures of 423, 523, and 623 K for 0.5 h. Then, the CE charges were measured after cooling to room temperature. As shown in Fig. 1(b), the triboelectric charges, which were generated by contacting with the conductive tip, induced the film surface potential changes  $\Delta V$  of 15, -4, and -13 mV, and they correspond to surface charge densities  $\sigma$  of 91, -24, and -79  $\mu\text{C}/\text{m}^2$ , respectively.<sup>18</sup> It should be noted that, with the increase in the sample annealing temperature, the CE charges on the surface measured at room temperature

turned from positive to negative. Even after annealing at 623 K for 0.5 h, the film is still amorphous and no crystal phase formation is found [Fig. 1(c)], though the surface topography is slightly coarser than that after annealing at 423 and 523 K (see [supplementary material](#) Fig. S1). As shown in the Fourier transform infrared spectra (FTIR) [Fig. 1(d)], there are many functional groups in the film after annealing at 423 K, including the C=O stretching vibration peak at  $1730\text{ cm}^{-1}$ , the -CH<sub>3</sub> bending vibration peak at  $1381\text{ cm}^{-1}$ , and the Nb–O–Nb peaks at 803 and  $674\text{ cm}^{-1}$ .<sup>19–23</sup> After annealing at 623 K, the peak of C=O basically completely disappears, and those of Nb–O–Nb and Nb–O become broadened. As shown in the x-ray photoelectron spectroscopy (XPS) results of Nb 3d [Fig. 1(e)], the binding energies of Nb 3d<sub>5/2</sub> and Nb 3d<sub>3/2</sub> are 207.1 and 209.9 eV, respectively. As shown in Fig. 1(f), there are peaks of Nb–O–Nb at 530.2 eV, Nb–OC at 531.6 eV, and Nb–OH at 533.4 eV, respectively, after the peak split of O 1s. As the annealing temperature rises, the proportion of Nb–O–Nb gradually grows, while those of Nb–OC and Nb–OH representing organic matter gradually fall. In addition, according to the energy difference,  $\Delta(\text{O–Nb}) = \text{BE}(\text{O } 1s) - \text{BE}(\text{Nb } 3d_{5/2}) = 323.1\text{ eV}$ , all of the Nb in the films should be of +5 valence after annealing.<sup>24</sup> As the annealing temperature increases, the molar ratio of O/Nb decreases from 5.49 to 4.97, and finally to 3.45, which is indeed higher than the stoichiometric

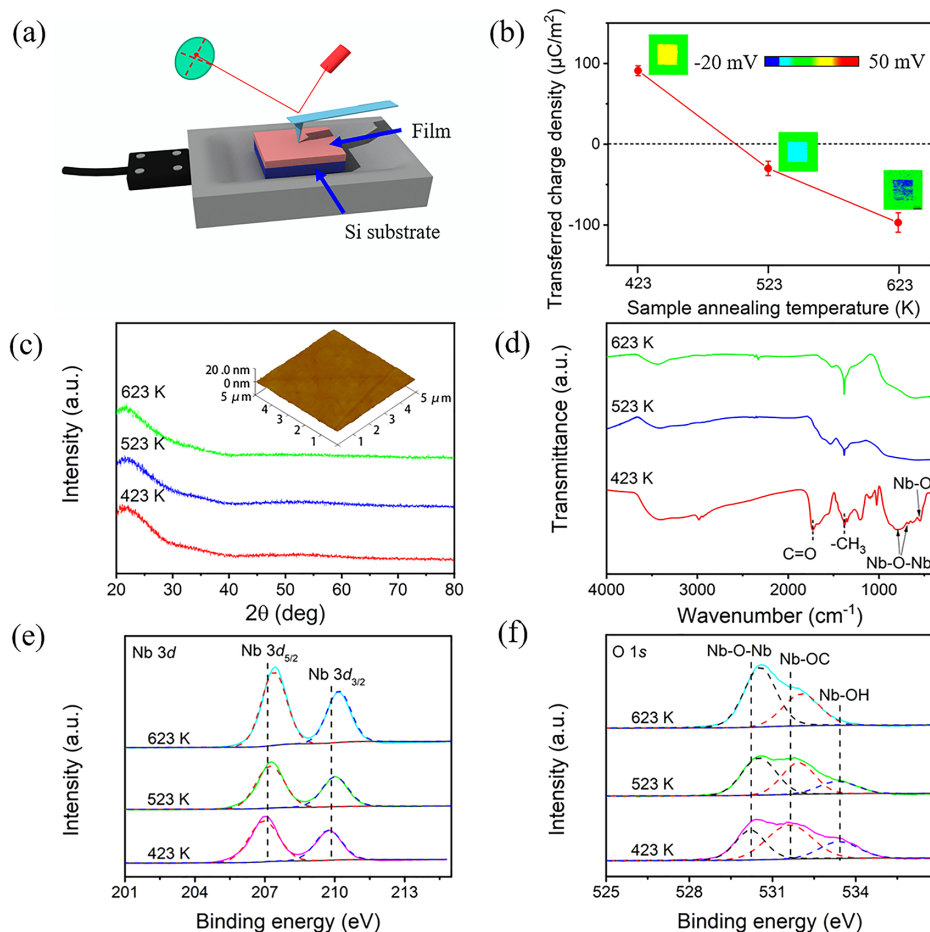


**FIG. 1.** (a) The generation of the triboelectric charges on the film surface by using the KPFM mode. (b) The triboelectric charges under the room temperature on Nb<sub>2</sub>O<sub>5</sub> films after the samples being annealed at different temperatures. (c) XRD results of the films and inset is the surface topography of the film annealed at 623 K. (d) FTIR results of the films. XPS results of (e) Nb 3d and (f) O 1s of the films.

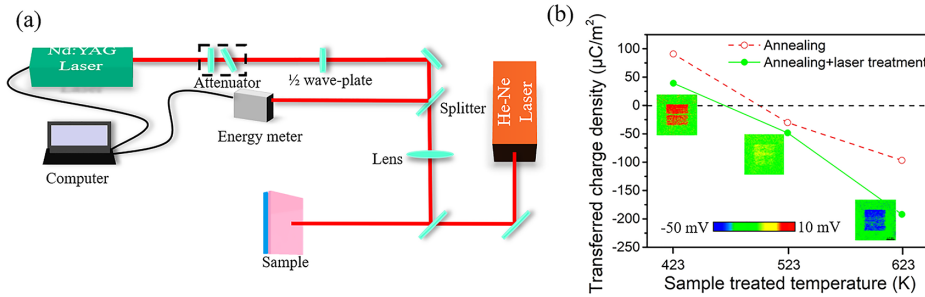


**FIG. 2.** (a) Setup of the laser irradiation platform. (b) The triboelectric charge transfer measured at room temperature after  $\text{Nb}_2\text{O}_5$  films being laser irradiated.

ratio of 2.50 due to the presence of oxygen-containing organic compounds in the film (see [supplementary material](#) Table 1).

The next experiment is aimed at the investigation of the effect of laser irradiation on CE. In [Fig. 2\(a\)](#), the nanosecond laser irradiation platform with a 1064 nm and 12 ns Nd:YAG laser is shown. The radiation laser energy was about  $1 \text{ J cm}^{-2}$ . Since the silicon is a high absorption substrate and the sol-gel film is highly transparent, laser irradiation plays a role similar to rapid thermal annealing. The annealed samples [red dashed line, [Fig. 2\(b\)](#)] are further treated with laser irradiation [solid blue line, [Fig. 2\(b\)](#)], and all of the triboelectric charges shift to the negative direction, sharing much consistency with the phenomenon in [Fig. 1\(b\)](#). This is because the temperature on the Si substrate may be much higher than 623 K due to the extremely high energy of laser irradiation, and such high temperature leads to a certain amount of negative charges in all the samples disregarding their annealing temperatures.

$\text{ZrO}_2$  films were prepared by the sol-gel method and then were annealed at 353, 423, 523, and 623 K for 0.5 h. The charge density is  $332 \mu\text{C}/\text{m}^2$  at 353 K [[Fig. 3\(a\)](#)], which drops to  $258 \mu\text{C}/\text{m}^2$  at 423 K,

$-58 \mu\text{C}/\text{m}^2$  at 523 K, and finally  $-92 \mu\text{C}/\text{m}^2$  at 623 K. It is noted that changes in charge densities and characteristics of the  $\text{ZrO}_2$  film after annealing are consistent with those of the  $\text{Nb}_2\text{O}_5$  films, namely, gradually reduced positive charges and emerging negative charges. In addition, due to the low phase transition temperature of  $\text{ZrO}_2$ , weak diffraction peaks appear in the XRD patterns (see [supplementary material](#) Fig. S2 may be a tetragonal (101) crystal plane.<sup>25</sup> According to the FTIR spectra [[Fig. 3\(b\)](#)], there are many functional groups in the film after annealing at 353 K, including the conjugated C=O stretching vibration peak at  $1597 \text{ cm}^{-1}$ , the C=C stretching vibration peak at  $1527 \text{ cm}^{-1}$ , the C-O stretching vibration peak at  $1026 \text{ cm}^{-1}$ , the  $-\text{CH}_3$  bending vibration peak at  $1381 \text{ cm}^{-1}$ , and the Zr-O peaks at  $772$  and  $636 \text{ cm}^{-1}$ .<sup>26</sup> As the annealing temperature increases, the peaks of functional groups gradually weaken. After annealing at 523 K, the C=O peak completely disappears; after annealing at 623 K, the C-O peak also disappears, whereas the Zr-O peaks become broadened. However, similar to the case in  $\text{Nb}_2\text{O}_5$  films, there are still a small amount of organic functional groups in the film, such as  $-\text{CH}_3$  and C=C, even after annealing at 623 K. As the annealing temperature

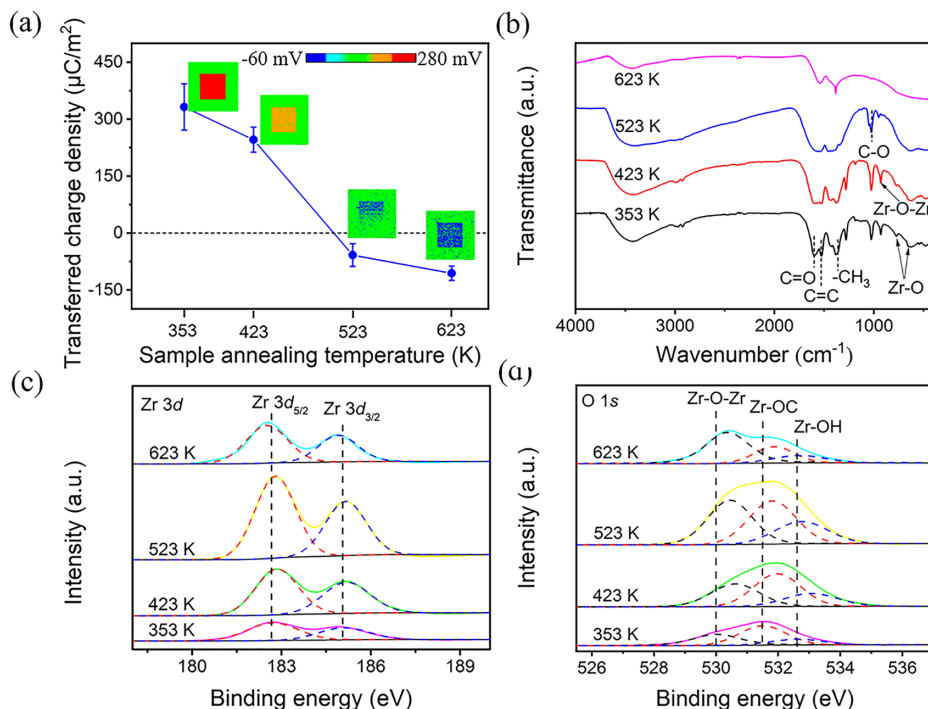


**FIG. 3.** (a) The triboelectric charges under the room temperature on  $\text{ZrO}_2$  films after treated at different temperatures. (b) FTIR results of the films. XPS results of Zr 3d (c) and O 1s (d) of the films.

risers, there are only slight shifts of Zr  $3d_{5/2}$  and Zr  $3d_{3/2}$  components in the XPS spectra [Fig. 3(c)]. According to the observation of the O 1s spectrum [Fig. 3(d)], the oxygen-contained bonds include the Zr–O–Zr bonds with a binding energy of 530.0 eV, Zr–OC bonds with a binding energy of 531.5 eV, and Zr–OH bonds with a binding energy of 532.6 eV. The proportion of Zr–O–Zr gets elevated as the annealing temperature rises, which indicates a decrease in organic matter content. Here, Zr  $3d_{5/2}$  has a binding energy of 182.7 eV, which corresponds to zirconium in the  $Zr^{4+}$  state.<sup>27,28</sup> It is seen in Table 2 (supplementary material) that the O/Zr ratio decreases from 4.61 to 3.69 as the annealing temperature increases, and it suggests the generation of more oxygen vacancies at higher temperatures. Moreover, sol–gel  $HfO_2$  films were prepared with  $HfCl_4$  as the precursor and acetylacetonate as the additive, followed by annealing at different temperatures from 353 to 623 K. Disregarding the low charge density on the surface of the  $HfO_2$  film, it is clearly seen that positive charges gradually reduce, while negative charges

gradually emerge, as the sample annealing temperature increases (see supplementary material Fig. S3).

It has been demonstrated in this study that CE on the organic–inorganic composite films is accompanied by the first emergence of positive charges and subsequent transition to low positive charges and finally negative charges as the annealing temperature increases. Based on the experimental data, it is speculated that some valence bonds in organics or organic–inorganic composites in the film are broken due to high temperature, which result in escaping of some internal carbon-containing functional groups. During this process, the oxygen content in the film reduced, resulting in oxygen vacancy defects. The emergence of these defects changes the film surface states, whose strong electron-withdrawing characteristics are considered to be the most important reason for the change in the electrification characteristics of the film. Here, we propose a surface states model to elaborate CE mechanisms of metal and dielectric annealed at different temperatures. Figures 4(a)–4(c) schematically illustrate electron transfer between the

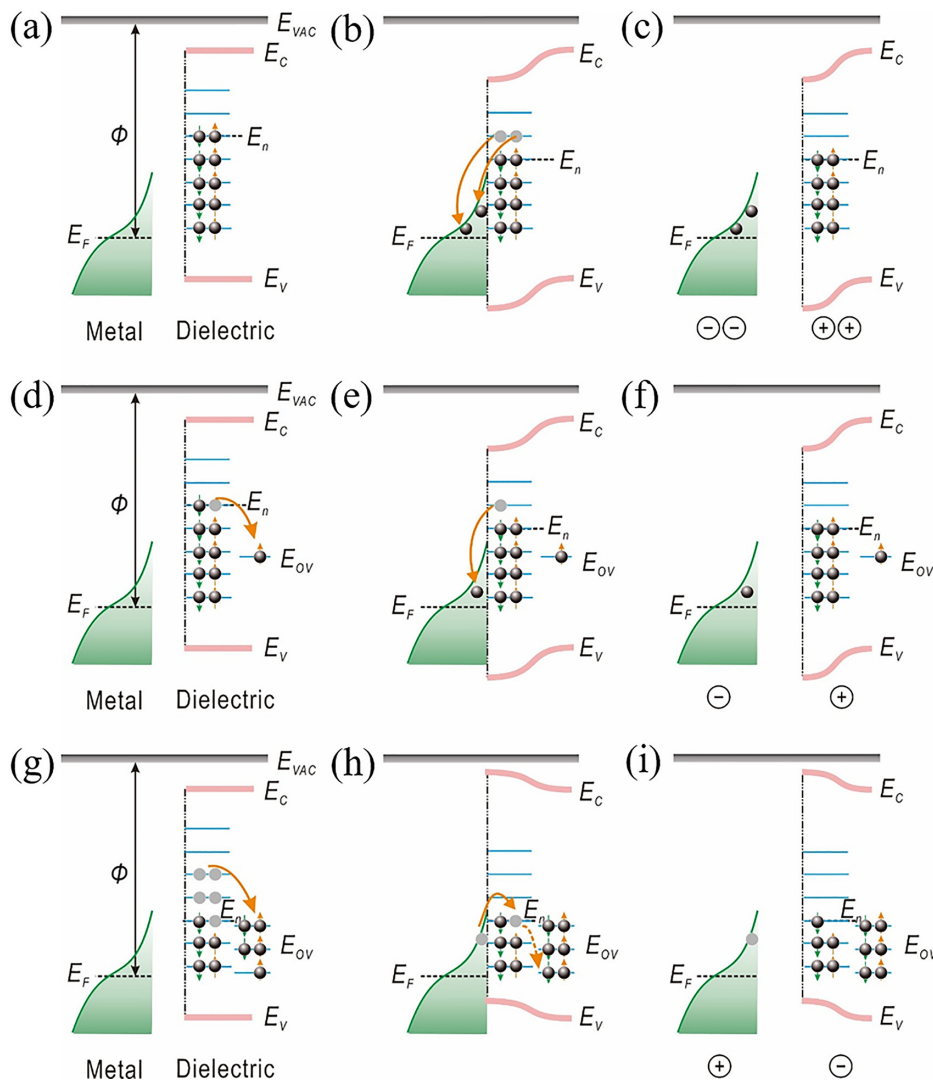


**FIG. 4.** Surface states model for explaining charge transfer between the metal and dielectric after (a)–(c)  $T_1$  annealing, (d)–(f)  $T_2$  annealing, (g)–(i)  $T_3$  annealing.  $\Phi$ , metal work function;  $E_F$ , Fermi level;  $E_{vac}$ , vacuum level;  $E_C$ , conduction band;  $E_n$ , neutral level of surface states;  $E_v$ , valence band;  $E_{OV}$ , level of oxygen vacancy;  $T_1 < T_2 < T_3$ .

metal and dielectric before, during, and after their contact after annealing at lower temperature  $T_1$ . The metal has a work function  $\Phi$ , and its electron distribution conforms to the Fermi–Dirac distribution function. The dielectric has a large  $E_n$  before contact with the metal, which is much higher than the energy level occupied by the electrons in the metal. When the two materials are in contact, electrons in the dielectric will jump into the metal, resulting in an  $E_n$  that is identical to the highest energy level occupied by electrons in the metal. When the two materials are separated, the dielectric is positively charged, while the metal is negatively charged, thereby resulting in CE. As the annealing temperature rises to  $T_2$ , oxygen vacancies are generated due to decomposition of some organic matter in the dielectric. The electron-withdrawing characteristics of oxygen vacancies may cause surface electrons to transit to these vacancies, resulting in changes in their surface states [Fig. 4(d)]. In this case, when two materials are in contact with each other, the number of electrons that are capable of transitioning from the surface to the metal gets reduced [Fig. 4(e)]. As a result, the amount of negative charges gained by the metal is lowered, while the amount of positive charges carried by the dielectric is also reduced [Fig. 4(f)]. As the annealing temperature is further increased to  $T_3$ , more oxygen vacancies appear in the dielectric, allowing more electrons to transition from the surface to these vacancies, which triggers more intense surface states' changes [Fig. 4(g)]. Such surface states' changes occur even when the two materials are in contact. Specifically, during the contact process, electrons in the metal transition to the dielectric, due to decrease in  $E_n$ . Moreover, these electrons that have transitioned to the dielectric may further transition to oxygen vacancies [Fig. 4(h)]. When separated, the metal is positively charged, while the dielectric is negatively charged. In other words, as the annealing temperature increases, not only the triboelectric charge quantity changes, but also the charge characteristic reverses [Fig. 4(i)].

In this study, we prepare organic–inorganic composite films by the sol–gel method, including  $\text{Nb}_2\text{O}_5$ ,  $\text{ZrO}_2$ , and  $\text{HfO}_2$  films. After annealing at different temperatures, positive triboelectric charges on the films gradually become negative ones. According to the results, valence bonds in organic or organic–inorganic composites in the film are broken at high temperature, resulting in oxygen vacancy defects that change the film surface states and further change electrification characteristics. Accordingly, we propose a model to elucidate the CE between the metal and dielectric after different temperature annealing, followed by detailed explanations about the mechanism. The findings in this paper provide an idea for controlling the CE and further changing the output of the TENGs.

See the [supplementary material](#) for more experimental details.

#### AUTHORS' CONTRIBUTIONS

Y.Z., S.L., and W.G. contributed equally to this work.

C. Xu thanks the Fundamental Research Funds for the Central Universities (No. 2019ZDZY05).

#### DATA AVAILABILITY

The data that support the findings of this study are available from the corresponding authors upon reasonable request.

#### REFERENCES

- F. R. Fan, Z. Q. Tian, and Z. L. Wang, *Nano Energy* **1**, 328 (2012).
- Z. L. Wang, *Mater. Today* **20**, 74 (2017).
- Z. L. Wang and A. C. Wang, *Mater. Today* **30**, 34 (2019).
- J. Lowell and A. C. Rose-Innes, *Adv. Phys.* **29**, 947 (1980).
- J. Lowell, *J. Phys. D: Appl. Phys.* **10**, 65 (1977).
- D. A. Hays, *J. Chem. Phys.* **61**, 1455 (1974).
- J. Lowell, *J. Phys. D: Appl. Phys.* **8**, 53 (1975).
- W. R. Harper, *Proc. R. Soc. London, Ser. A* **205**, 83 (1951).
- H. Baytekin, A. Patashinski, M. Branicki, B. Baytekin, S. Soh, and B. A. Grzybowski, *Science* **333**, 308 (2011).
- C. Xu, Y. Zi, A. C. Wang, H. Zou, Y. Dai, X. He, P. Wang, Y. Wang, and Z. L. Wang, *Adv. Mater.* **30**, 1706790 (2018).
- C. Xu, B. B. Zhang, A. C. Wang, W. Z. Cai, Y. L. Zi, P. Z. Feng, and Z. L. Wang, *Adv. Funct. Mater.* **29**, 1903142 (2019).
- C. Xu, A. C. Wang, H. Y. Zou, B. B. Zhang, C. L. Zhang, Y. L. Zi, L. Pan, P. H. Wang, P. Z. Feng, Z. Q. Lin, and Z. L. Wang, *Adv. Mater.* **30**, 1803968 (2018).
- Y. S. Zhou, S. Wang, Y. Yang, G. Zhu, S. Niu, Z. H. Lin, Y. Liu, and Z. L. Wang, *Nano Lett.* **14**, 1567 (2014).
- S. Q. Lin, L. Xu, L. P. Zhu, X. Y. Chen, and Z. L. Wang, *Adv. Mater.* **31**, 1901418 (2019).
- S. Q. Lin, L. Xu, C. Xu, X. Y. Chen, A. C. Wang, B. B. Zhang, P. Lin, Y. Yang, H. B. Zhao, and Z. L. Wang, *Adv. Mater.* **31**, 1808197 (2019).
- X. Wen, Y. Su, Y. Yang, H. Zhang, and Z. L. Wang, *Nano Energy* **4**, 150 (2014).
- C. X. Lu, C. B. Han, G. Q. Gu, J. Chen, Z. W. Yang, T. Jiang, C. He, and Z. L. Wang, *Adv. Eng. Mater.* **19**, 1700275 (2017).
- Y. S. Zhou, Y. Liu, G. Zhu, Z. H. Lin, C. F. Pan, Q. S. Jing, and Z. L. Wang, *Nano Lett.* **13**, 2771 (2013).
- Z. Huaxu, L. S. Hua, P. M. Tahir, Z. Ashaari, S. S. O. Al-Edrus, N. A. Ibrahim, L. C. Abdullah, and S. F. Mohamad, *Polymers* **13**, 98 (2020).
- F. T. Aquino, J. L. Ferrari, S. J. L. Ribeiro, A. Ferrier, P. Goldner, and R. R. Goncalves, *Opt. Mater.* **35**, 387 (2013).
- L. A. Rodrigues and M. L. C. P. da Silva, *J. Non-Cryst. Solids* **356**, 125 (2010).
- M. Ristic, S. Popovic, and S. Music, *Mater. Lett.* **58**, 2658 (2004).
- K. V. Baiju, S. Shukla, K. S. Sandhya, J. James, and K. G. K. Warriar, *J. Sol-Gel Sci. Technol.* **45**, 165 (2008).
- V. V. Atuchin, I. E. Kalabin, V. G. Kesler, and N. V. Pervukhina, *J. Electron Spectrosc. Relat. Phenom.* **142**, 129 (2005).
- C. Xu, P. Yi, H. Fan, J. Qi, Y. Qiang, J. Liu, C. Tao, and D. Li, *Appl. Surf. Sci.* **289**, 141 (2014).
- W. M. Xia, N. Li, B. Deng, R. Y. Zheng, and Y. Q. Chen, *Ceram. Int.* **45**, 11062 (2019).
- O. A. Bulavchenko, Z. S. Vinokurov, T. N. Afonassenko, P. G. Tsyryl'nikov, S. V. Tsybulya, A. A. Saraev, and V. V. Kaichev, *Dalton Trans.* **44**, 15499 (2015).
- M. Ismail, M. K. Rahmani, S. A. Khan, J. Choi, F. Hussain, Z. Batool, A. M. Rana, J. Lee, H. Cho, and S. Kim, *Appl. Surf. Sci.* **498**, 143833 (2019).